

# Effects of changes of osteocyte shape on fluid flow and fluid shear stress of loaded bone

WeiLun Yu (✉ [weilun1990@163.com](mailto:weilun1990@163.com))

Taiyuan University of Technology <https://orcid.org/0000-0002-6253-576X>

Xuyang Huo

Jilin Medical University

Hongliang Li

Jilin Medical University

Fengjian Yang

Jilin Medical University

Qiuju Qi

Jilin Medical University

Xiaogang Wu

Taiyuan University of Technology

Weiyi Chen

Taiyuan University of Technology

---

## Research

**Keywords:** pressure gradient, osteocyte, Poroelasticity, pore pressure, fluid shear stress, permeability

**Posted Date:** April 21st, 2022

**DOI:** <https://doi.org/10.21203/rs.3.rs-454657/v2>

**License:**  This work is licensed under a Creative Commons Attribution 4.0 International License.

[Read Full License](#)

---

# 1 **Effects of osteocyte shape on fluid flow and** 2 **fluid shear stress of the loaded bone**

3 Yang Fengjian<sup>1</sup>; Yu Weilun<sup>1\*</sup>; Huo Xuyang<sup>1</sup>; Li Hongliang<sup>1</sup>; Qi Qiuju<sup>1</sup>; Yang

4 Xiaohang<sup>1</sup>; Shi Nianqiu; Xiaogang Wu; Weiyi Chen

5 <sup>1</sup>College of Biomedical Engineering, Jilin Medical University, Jilin, Jilin, China

6 <sup>2</sup>Collage of Biomedical Engineering, Taiyuan University of Technology, Taiyuan,  
7 Shanxi Province, China

8

9 *Corresponding author: \*Dr. Yu Weilun, College of Biomedical Engineering, Jilin*  
10 *Medical University, Jilin 132013, China; Email: weilun1990@163.com.*

## 11 **Abstract**

12 This study was conducted to better understand the specific behavior of the  
13 intraosseous fluid flow. We calculated the number and distribution of bone canaliculi  
14 around the osteocytes based on the varying shapes of osteocytes. We then used these  
15 calculated parameters and other bone microstructure data to estimate the anisotropy  
16 permeability of the lacunar-canalicular network. Poroelastic finite element models of  
17 the osteon were established, and the influence of the osteocyte shape on the fluid flow  
18 properties of osteons under an axial displacement load was analyzed. Two types of  
19 boundary conditions (BC) that might occur in physiological environments were  
20 considered on the cement line of the osteon. BC1 was allows free fluid passage from  
21 the outer elastic restraint boundary, and BC2 was impermeable outer displacement  
22 constrained boundary. They both have the same inner boundary conditions allow fluid

23 to pass through. Changes in the osteocyte shape altered the maximum value of  
24 pressure gradient (PG), pore pressure (PP), fluid velocity (FV), and fluid shear stress  
25 (FSS) relative to the reference model (spherical osteocytes). The maximum PG, PP,  
26 FV, and FSS in BC2 were nearly 100% larger than those in BC1, respectively. It is  
27 found that the BC1 was closer to the real hysiological environment. The anisotropy of  
28 fluid flow along different directions in the elongated osteocyte model was more  
29 evident than that in other models, which may have been due to the large difference in  
30 permeability along different directions. Changes in osteocyte shape significantly  
31 affect the degrees of anisotropy of fluid flow and porous media of the osteon. The  
32 model presented in this study can accurately quantify fluid flow in the  
33 lacunar-canalicular network.

34 **Keywords:** pressure gradient; osteocyte; poroelasticity; pore pressure; fluid  
35 shear stress; permeability

## 36 **1 Introduction**

37 The cortical bone contains two hierarchical structures of interconnected channels.  
38 The larger system comprises Haversian and Volkmann's canals, and the smaller one  
39 is the lacunar-canalicular network. Osteocytes are bathed in the interstitial fluid of the  
40 lacunar-canalicular porosity, and mechanical loading drives the free fluid in and out  
41 of the pore by inducing bone matrix deformation[1]. The pore pressure gradient[2, 3],  
42 solute transport[4, 5], and fluid shear stress generated by the fluid flow are considered  
43 to be significant biomedical signals for osteocyte mechanotransduction in situ[6, 7,

44 8]Osteocytes are the most sensitive bone cell type that considered as mechanosensors  
45 within bone that can sense mechanical stimulations and transduce them into  
46 biochemical signals[9], thereby regulating bone remodeling[10, 11], however whether  
47 and how these factors generated by the fluid flow as a flow sensor to activate the  
48 native osteocyte remains unclear[12]. Strain amplification effect on osteocyte  
49 membrane may produce a less osteogenic thanresponse than fluid flow[13], and some  
50 studies have suggested that the fluid flow shears the osteocyte membranes or induces  
51 cytoskeleton deformation to elicit biochemical responses[1, 6, 8] [14].In addition, the  
52 primary cilium and integrin from osteocytes may be a mechanosensor under the fluid  
53 flow[13, 15]. However, osteocytes are embedded in a mineralized extracellular matrix,  
54 making it difficult to apply direct experimental approaches. Therefore, mathematical  
55 models of fluid flow in the bone matrix have been established[16, 17, 18, 19].  
56 Poroelasticity is a well-developed concept for investigating the interaction of fluid  
57 and solid phases in the bone[3, 20, 21, 22]. Permeability is an important index to  
58 describe fluid flow, it determines how fast fluid can flow through the pores..  
59 Numerical simulation can be used to explore the fluid flow induced by mechanical  
60 loading and calculate the values of pore pressure (PP), fluid velocity (FV), and fluid  
61 shear stress (FSS) in the bone using the poroelastic model [3, 4, 7, 8, 22]. Compared  
62 with the isotropic model (i.e., osteocytes are spherical), the anisotropic model can  
63 more accurately reflect the specific microstructure of bone[23], such as the shape,  
64 direction, and density of lacunar-canalicular network[24]...

65 In recent years, the spatial characteristics of osteocytes including morphology

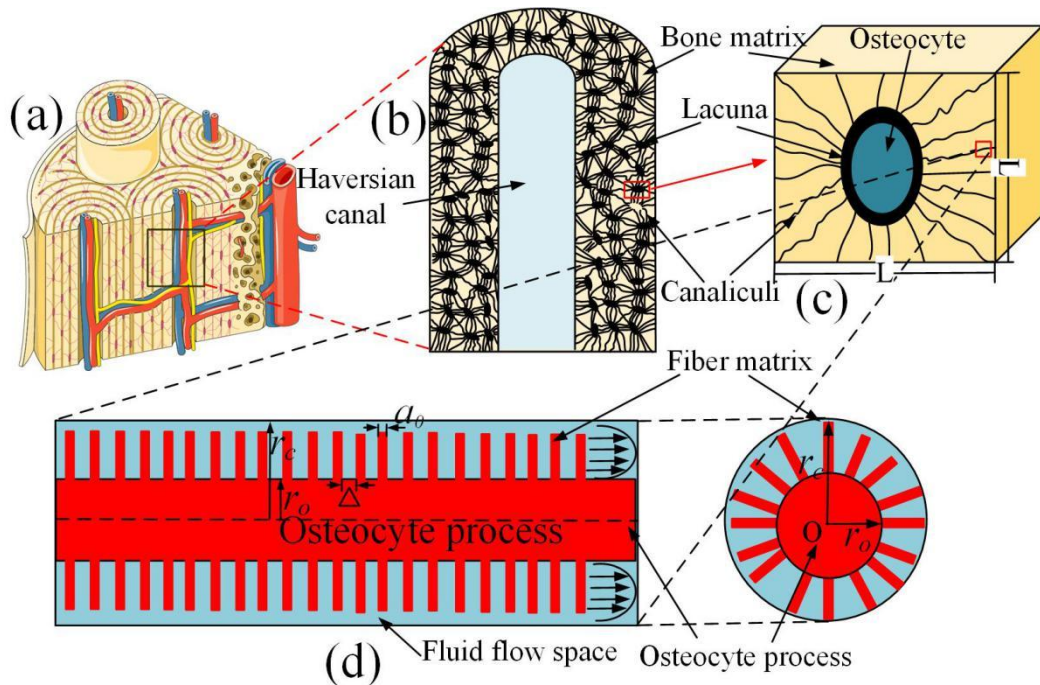
66 and orientation and the potential relationship between these characteristics and disease  
67 have gained importance [11, 24, 25, 26]. In vitro experiments indicate that the  
68 osteocyte geometry affects its strain response [25, 27]. Carter et al. found that the  
69 density, shape, and orientation of the osteocytes in the anterior, posterior, medial, and  
70 lateral femur significantly differ probably because of local changes in the load [24].  
71 Recent studies have shown that the osteocytes of osteoporosis patients are more  
72 irregular and the bone canaliculi are more curved than normal; the FSS and FV on the  
73 osteocyte membrane are also greatly altered [28]. Age is an important factor affecting  
74 the shape of osteocytes [29]. As age increases, the surface area of osteocytes  
75 decreases and the osteocytes flatten [30]. Changes in osteocyte morphology can  
76 determine the changes of the three-dimensional distribution of bone canalicules ,  
77 resulting in anisotropic permeability of bone tissue. [31]. In the finite element analysis  
78 of poroelasticity, it is necessary to accurately quantify the permeability of the  
79 lacunar-canalicular network to capture the anisotropic fluid flow behavior of the bone.

80 Therefore, to more accurately elucidate the specific behavior of intraosseous  
81 fluid flow, we developed a poroelastic finite element model based on the  
82 microstructure of the bone tissue. First, a three-dimensional bone permeability  
83 analysis was performed according to the three-dimensional distribution of bone  
84 canalicules calculated from osteocyte shape. Then, based on the theory of  
85 poroelasticity, a finite element model of osteons was established to calculate the fluid  
86 flow behavior under an axial load. The results are expected to improve our  
87 understanding of the mechanism of bone conduction and bone functional adaptation.

88 **2. Material and Methods**

89 **2.1. Calculation of osteon permeability based on osteocyte**  
90 **shape**

91 The interstitial bone and an osteon cluster are shown in Fig. 1a. A single osteon  
92 (among the cluster shown in Fig. 1a) is shown in Fig. 1b. Assuming a regular  
93 arrangement of the lacunar-canalicular network (Fig. 1b) and uniform distribution of  
94 the bone canaliculi, osteons can be considered to compose the cube periodic unit cells  
95 (CPUC) that surround the osteocyte lacuna (Fig. 1c). Fig. 1d is The microstructure of  
96 the canaliculus is shown in Fig. 1d;  $r_c$  is the radius of the canaliculus,  $r_o$  is the radius  
97 of the osteocyte process, and  $a_0$  is the radius of the fiber matrix around the osteocyte  
98 process.



99

100

Fig. 1 The hierarchical structure of the bone tissue

101

102

Expanding the Weinbaum et al. model to account for the 3-D distribution of the

103 canaliculi, the lacunar-canalicular permeability,  $k_{lcp}$ , was calculated based on the  
 104 anatomical features of the lacuna-canalicular network as follows [7]:

$$105 \quad k_{lcp} = \frac{2\pi n_i a^4 q^3}{\gamma^3 L^2} \left\{ A_1 \left[ I_1\left(\frac{\gamma}{q}\right) - q I_1(\gamma) \right] + B_1 \left[ q K_1(\gamma) - K_1\left(\frac{\gamma}{q}\right) \right] + \frac{\gamma(q^2 - 1)}{2q} \right\} \quad (1)$$

106  $q$  is the dimensionless ratio between  $r_c$  (0.23 $\mu$ m) and  $r_o$  (0.1 $\mu$ m) ( $q = r_c/r_o$ ).  $\gamma$  is  
 107 a dimensionless length ratio between the  $r_c$  and the square root of the small-scale  
 108 permeability ( $k_p$ ) constant for the fluid annulus, which is filled with a fiber  
 109 matrix  $\gamma = b/\sqrt{k_p}$ , and  $k_p = 0.0572a_0^2(\Delta/a_0)^{2.377}$ , where  $a_0$  is the radius of the  
 110 pericellular fibers (5 nm), and  $\Delta$  is the effective spacing of the fibers of the  
 111 pericellular matrix (7 nm) [7, 17, 31].

112  $A_1$  and  $B_1$  can be obtained from the following equation:

$$113 \quad A_1 = \frac{K_0(\gamma) - K_0(\gamma/q)}{I_0(\gamma/q)K_0(\gamma) - I_0(\gamma)K_0(\gamma/q)} \quad (2)$$

$$B_1 = \frac{I_0(\gamma) - I_0(\gamma/q)}{I_0(\gamma/q)K_0(\gamma) - I_0(\gamma)K_0(\gamma/q)}$$

114  $I_n$  and  $K_n$  denote the first and the second modifications of the Bessel function of  
 115 order  $n$ , respectively.

116  $L$  represents the distance between two bone lacunae, which is also the side length  
 117 of CPUC. It can be obtained from the following formula:

$$118 \quad L = \left( \frac{V_L}{N_{Lac}} \right)^{\frac{1}{3}} \quad (3)$$

119  $V_L$  represents unit volume, and  $N_{Lac}$  represents the number of lacunae per  $\text{mm}^3$  of  
 120 bone unit volume. The range of  $N_{Lac}$  is  $26\text{--}90 \times 10^3$  ( $N_{Lac}/\text{mm}^3$ ) [24, 32]. In this study,  
 121 the  $N_{Lac}$  value of unit volume was selected as  $37 \times 10^3$ , so that the value of  $L$  was 30 $\mu$ m.

122 According to the literature, the average number of bone canaliculi around each bone  
 123 lacuna is  $N = 62$  [33]. Because the morphology of osteocytes is similar to an ellipsoid,  
 124 we used the standard equation of an ellipsoid to represent the osteocyte.

$$125 \quad \frac{x^2}{a^2} + \frac{y^2}{b^2} + \frac{z^2}{c^2} = 1 \quad (4)$$

126 The long half axis is  $a$ , middle half axis is  $b$ , and short half axis is  $c$ . The porosity of  
 127 the lacunar-canalicular network can be expressed by the following formula:

$$128 \quad \varphi = \frac{N\pi(r_c^2 - r_o^2)Lc + \frac{4}{3}\pi abc}{L^3} \quad (5)$$

129  $L_C$  is the average length of the bone canaliculi.

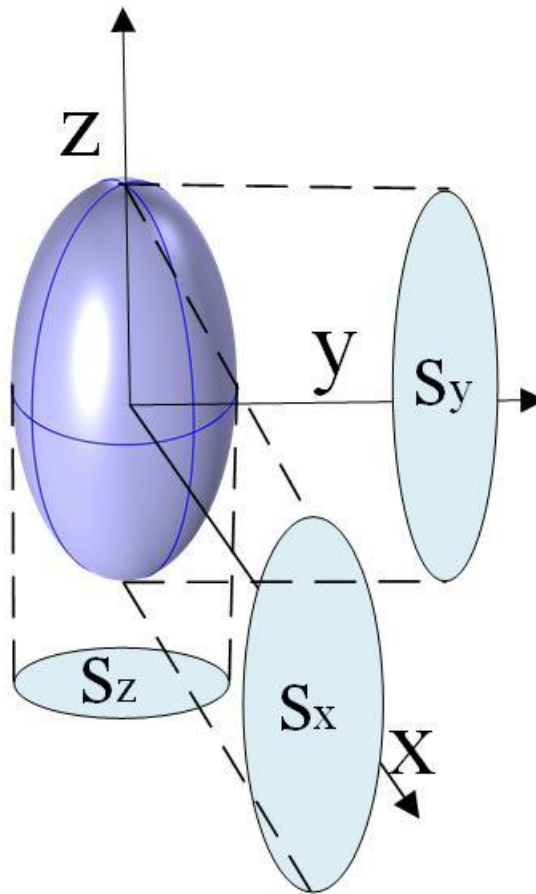
130 We regarded the whole bone lacuna space and osteocyte body as one pore space.

131 Weinbaum et al. assumed that the number of canaliculi passing through the surface of  
 132 the CPUC in each principal direction was the same [7]. However, because of  
 133 differences in the osteocyte shape, the number of canaliculi ( $n_i$ ) crossing each face of  
 134 the CPUC will be anisotropic [31]. As shown in Fig. 2, the 3-D distribution of the  
 135 canaliculi was based on the projection surface area of the osteocyte shape. The  
 136 number of canaliculi in the different directions could be measured by the projection  
 137 area ratio of the osteocyte [31]:

$$138 \quad \begin{cases} n_x = \frac{1}{2} \frac{S_x}{S_x + S_y + S_z} \times N \\ n_y = \frac{1}{2} \frac{S_y}{S_x + S_y + S_z} \times N \\ n_z = \frac{1}{2} \frac{S_z}{S_x + S_y + S_z} \times N \end{cases} \quad (6)$$

139  $n_x$ ,  $n_y$ , and  $n_z$  are the numbers of canaliculi parallel to the  $x$ (radial),  $y$ (tangential),

140 and  $z$ (axial) axes passing through each face of the CUPC, respectively;  $S_x$ ,  $S_y$ , and  $S_z$   
141 are projected surface areas of the bone lacuna in the  $x$ ,  $y$ , and  $z$  directions, respectively  
142 [31].



143  
144 Fig. 2. The projection area of osteocytes along the  $x$  axis ( $S_x$ ),  $y$  axis ( $S_y$ ), and  $z$   
145 axis ( $S_z$ ).

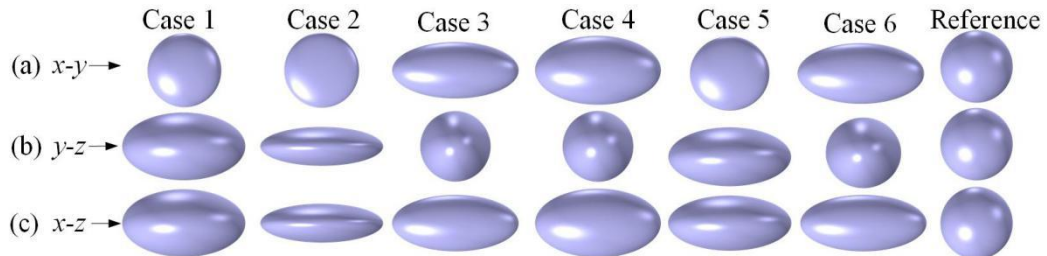
146

## 147 **2.2 Osteocyte shape**

148 To more clearly describe the shape of the osteocyte, we defined three  
149 eigenvalues  $EV_1$ ,  $EV_2$ , and  $EV_3$  ( $EV_1$  is the square of the long half axis,  $EV_2$  is the  
150 square of the middle half axis, and  $EV_3$  is the square of the short half axis) [24]. The  
151 shape parameters were then computed for each ellipsoid based on the resulting three  
152 EVs. Three ratios of the EV, degree of anisotropy ( $1-EV_3:EV_1$ ), degree of elongation

153 (1–EV2:EV1), and degree of flatness (1–EV3:EV2) were derived from studies of  
 154 particle shape to define the degree of difference. As shown in Table 1 and Fig. 3,  
 155 several groups of osteocytes with different indicators (anisotropy, elongation, and  
 156 flatness) were considered to observe the influence of osteocyte shape on the internal  
 157 fluid flow. Fig. 3 shows the importance of these three indicators on the shape of the  
 158 osteocyte.

159 When the three eigenvalues were equal (EV1 =EV2 = EV3), the osteocyte was  
 160 spherical (Reference). When EV1 = EV2 > EV3, the osteocyte was flat (Case 1 and  
 161 Case 2). When EV1 > EV2 = EV3, the osteocyte was elongated (Case 3 and Case 4).  
 162 When the three eigenvalues were different (EV1 > EV2 > EV3), the shape depended  
 163 on the extension length and flatness (Case 5 and Case 6).



164  
 165 Fig. 3 Representative cases of osteocyte shapes. The projected osteocyte shapes are  
 166 shown schematically in (a) the x-y plane, (b) the y-z plane, and (c) the x-z plane.

167

168 According to the osteocyte shape parameters (Table 1), the permeability values of  
 169 Case 1–Case 6 were denoted K1, K2, K3, K4, K5, and K6, respectively. The  
 170 permeability of the reference model was isotropic, and its value was  $1.05 \times 10^{-20} \text{ m}^2$ .

171

$$K1 = \begin{pmatrix} 8.25 \times 10^{-21} & & \\ & 8.25 \times 10^{-21} & \\ & & 1.50 \times 10^{-20} \end{pmatrix} m^2,$$

172 
$$K2 = \begin{pmatrix} 6.10 \times 10^{-21} & & \\ & 6.10 \times 10^{-21} & \\ & & 1.93 \times 10^{-20} \end{pmatrix} m^2,$$

173 
$$K3 = \begin{pmatrix} 5.74 \times 10^{-21} & & \\ & 1.29 \times 10^{-20} & \\ & & 1.29 \times 10^{-20} \end{pmatrix} m^2,$$

174 
$$K4 = \begin{pmatrix} 6.77 \times 10^{-21} & & \\ & 1.28 \times 10^{-20} & \\ & & 1.28 \times 10^{-20} \end{pmatrix} m^2,$$

175 
$$K5 = \begin{pmatrix} 7.31 \times 10^{-21} & & \\ & 7.84 \times 10^{-21} & \\ & & 1.64 \times 10^{-20} \end{pmatrix} m^2,$$

176 
$$K6 = \begin{pmatrix} 5.91 \times 10^{-21} & & \\ & 1.24 \times 10^{-20} & \\ & & 1.32 \times 10^{-20} \end{pmatrix} m^2,$$

177 Table 1 Geometry and degree of representative cases

	a	b	c	Degree of Anisotropy	Degree of Elongation	Degree of Flatness
Case 1	6.1	6.1	3.35	0.3	0	0.7
Case 2	7.34	7.34	2.32	0.1	0	0.9
Case 3	8.57	3.82	3.82	0.2	0.8	0
Case 4	7.47	4.09	4.09	0.3	0.7	0
Case 5	6.69	6.24	2.99	0.2	0.13	0.77
Case 6	8.36	4	3.74	0.2	0.77	0.12
Reference	5	5	5	1	0	0

179

## 2.3 Establishment of governing equation and finite element

180

### model of osteon governing equation

181

182 Due to the periodicity of the geometrical configuration, we defined the

183 representative elementary volume (REV) by CUPC. The poroelasticity theory

184 efficiently describes the fluid flow behavior of the osteon [3, 4, 7, 18, 34]. The osteon

185 was illustrated as a solid-liquid coupling porous elastic material composed of CUPC

186 units in this study. As shown in Fig. 4, the osteon was considered a hollow annular

187 cylinder under cyclic loading in the longitudinal orientation. The following governing

188 equations could describe the poroelastic behavior of the bone, and no body forces

189 were considered. Constitutive laws for the solid matrix material and the saturating

fluid were as follows [18]:

$$190 \quad \boldsymbol{\sigma} = \mathbf{C}\boldsymbol{\varepsilon} - \boldsymbol{\alpha}p \quad (7)$$

$$191 \quad p = M \left[ \xi - \text{tr}(\boldsymbol{\alpha}\boldsymbol{\varepsilon}) \right] \quad (8)$$

192  $\boldsymbol{\sigma}$  is the total stress tensor,  $\mathbf{C}$  is the drained stiffness tensor,  $\boldsymbol{\varepsilon}$  is the total strain

193 tensor,  $\boldsymbol{\alpha}$  is the Biot's effective stress tensor with the same principal orientations as

194 the compliance tensor,  $p$  is the  $PP$ , and  $M$  is the Biot modulus that links the fluid

195 content variation to the pressure in the absence of solid matrix deformations.  $\xi$  is the

196 variations in fluid content, and  $\text{tr}(\cdot)$  is the trace operator.

197 The equilibrium equation is given by:

$$198 \quad \rho \ddot{\mathbf{u}}^s - \nabla \cdot \boldsymbol{\sigma} = \mathbf{0} \quad (9)$$

199  $\rho$  is the total density, and  $\ddot{\mathbf{u}}^s$  is the second derivative of the displacement.

200 The fluid mass conservation equation is given by:

$$201 \quad \frac{\partial \xi}{\partial t} = -\nabla \cdot \mathbf{V} \quad (10)$$

202 Fluid flow was calculated by Darcy's law:

$$203 \quad \mathbf{V} = -\mathbf{k} \left( \nabla p + \rho_f \ddot{\mathbf{u}}^s \right) \quad (11)$$

204  $\mathbf{V}$  is the velocity vector, and  $\mathbf{k}$  is the anisotropic permeability tensor, i.e., the textural  
205 parameter allowing to quantify the ability of a porous material to transmit fluids  
206 through Darcy's law.

207 After neglecting body forces, the governing poroelastic equations for an  
208 anisotropic material in the low frequency range (such as walking, a few Hertz) were  
209 given by plugging (8) into (10) and plugging (9) and (12) into (11):

$$210 \quad \left. \begin{aligned} \boldsymbol{\alpha} \nabla p &= \nabla \cdot (\mathbf{M} \boldsymbol{\varepsilon}) \\ \frac{1}{M} \frac{\partial}{\partial t} p - \nabla \cdot (\mathbf{k} \nabla p) &= -\frac{\partial}{\partial t} [\text{tr}(\boldsymbol{\alpha} \boldsymbol{\varepsilon})] \end{aligned} \right\} \quad (12)$$

211

212 Given the low load frequency, the Haversian canal acts as a reservoir to maintain  
213 the normal fluid flow in and out. It was assumed that the vascular pores were no  
214 longer saturated, so the pressure on the surface of the Haversian canal was set to 0  
215 (reference pressure). The pore size of the Haversian canal was much larger than that  
216 of the bone canaliculus, so the Haversian canal provided space for the fluid pressure  
217 to relax when the bone was under mechanical load.

218 Two boundary conditions representing the physiological environment of the  
 219 osteon were considered. At the top and bottom of the osteon, the displacement  
 220 boundary conditions were applied to generate a cyclic compressive load of  $1000\mu\varepsilon$ ,  
 221 and the radial and tangential displacements were limited on the bottom to prevent  
 222 rigid displacement

223 BC1: the cement line of the osteon is not constrained by the interstitial tissue  
 224 around the osteon, and the liquid can flow in and out freely. The cement line was not  
 225 impermeable, and it affected by the time-dependent confining pressure  $p(t)(p(b, t))$ :

$$\begin{aligned}
 \sigma_{rr}^1 \Big|_{r=a} &= p^1 \Big|_{r=a} = 0 \\
 \sigma_{rr}^1 \Big|_{r=b} &= -p^1(t) \Big|_{r=b} \\
 \partial p^1 / \partial r \Big|_{r=b} &= 0
 \end{aligned} \tag{13}$$

227 BC2: the cement line was impermeable, and displacement was constrained:

$$\begin{aligned}
 \sigma_{rr}^2 \Big|_{r=a} &= p^2 \Big|_{r=a} = 0 \\
 u_r^2 \Big|_{r=b} &= 0 \\
 \partial p^2 / \partial r \Big|_{r=b} &= 0
 \end{aligned} \tag{14}$$

229 The FSS experienced by the osteocyte and its processes was obtained by the  
 230 following equation[21]:

$$FSS = \frac{8\mu v_r}{d} \tag{15}$$

232  $d$  is the mean pore diameter:

$$d = 4\sqrt{2Tk/\varphi} \tag{16}$$

234  $v_r$  is the interstitial fluid velocity, given by the Dupuit relation:

$$v_r = \frac{Tv}{\varphi} \tag{17}$$

236  $T$  is the tortuosity of the flow path ( $t = 1$  for straight channels), and  $v$  is the value of

237 Darcy velocity [21].

## 238 2.4 Model establishment and calculation

239 The COMSOL Multiphysics software was used to investigate the poroelastic  
240 behavior of the fluid -solid interaction in osteons under an axial compression load. As  
241 shown in Fig. 4a, the osteon was defined as a hollow cylinder composed of CPUC,  
242 and its material and geometric parameters are shown in Table 2.

243 Table 2 Geometrical and material constants used in the osteon model[19, 20, 22, 34]

Parameter	Description	Value
$E_r$	Radial drained Young's modulus	15.9 (GPa)
$\nu_r$	Radial drained Poisson's ratio	0.328
$E_z$	Axial drained Young's modulus	20.3 (GPa)
$\nu_z$	Axial drained Poisson's ratio	0.25
$M$	Biot's modulus	38 (GPa)
$a$	Biot's effective coefficient	0.132
$\rho_s$	Solid density	2000 (kg/m <sup>3</sup> )
$\rho_f$	Fluid density	1000 (kg/m <sup>3</sup> )
$\mu$	Dynamic viscosity	10 <sup>-3</sup> (Pa·s)
$R_a$	Inner radius of bone tissue	50 (μm)
$R_b$	Outer radius of bone tissue	150 (μm)
$C_p$	Fluid compressibility	4×10 <sup>-10</sup> (1/Pa)

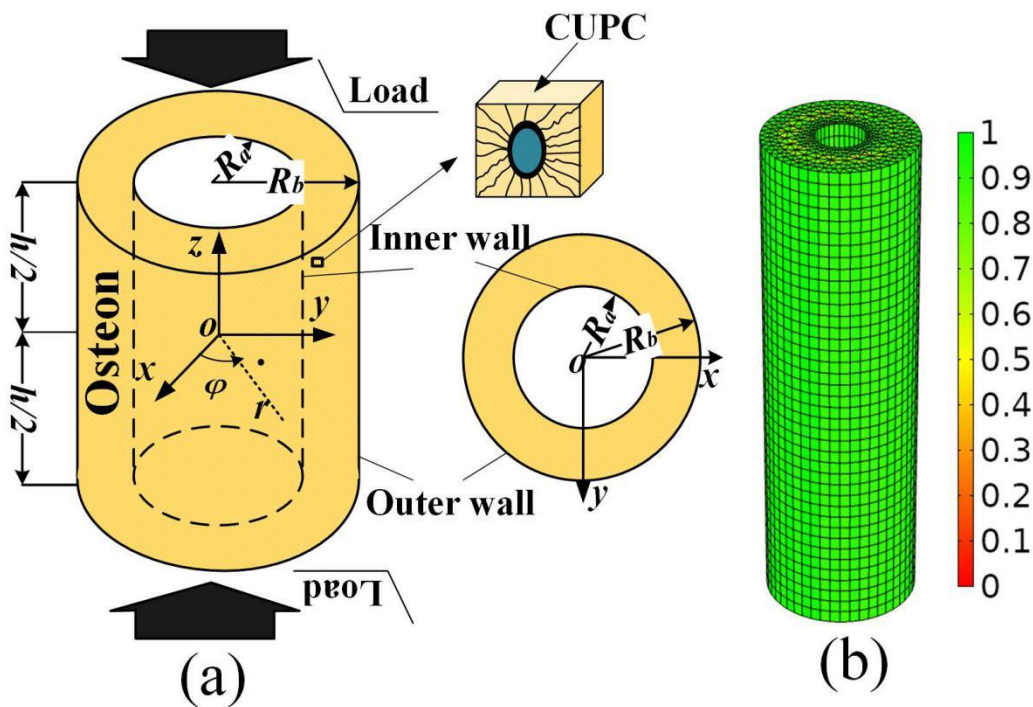
244

245 The compression loads on the top and bottom of the osteon were both  
246 represented by a harmonic displacement ( $w$ ) of amplitude 0.5 μm and a frequency  $f$ ,

247 which resulted in the maximum strain loading  $\varepsilon = 0.001$  at  $t = 0.5$  s, but the maximum  
 248 pressure and velocity responses were at  $t = 0.25$  s [22, 34]:

249 
$$w|_{z=\pm 0.5mm} = \pm 0.00025 [\cos(2\pi ft) - 1] [mm] \quad (18)$$

250 As shown in Fig. 4(b), the mesh used in the finite element simulation contained 20880  
 251 elements and 54277 degrees of freedom.

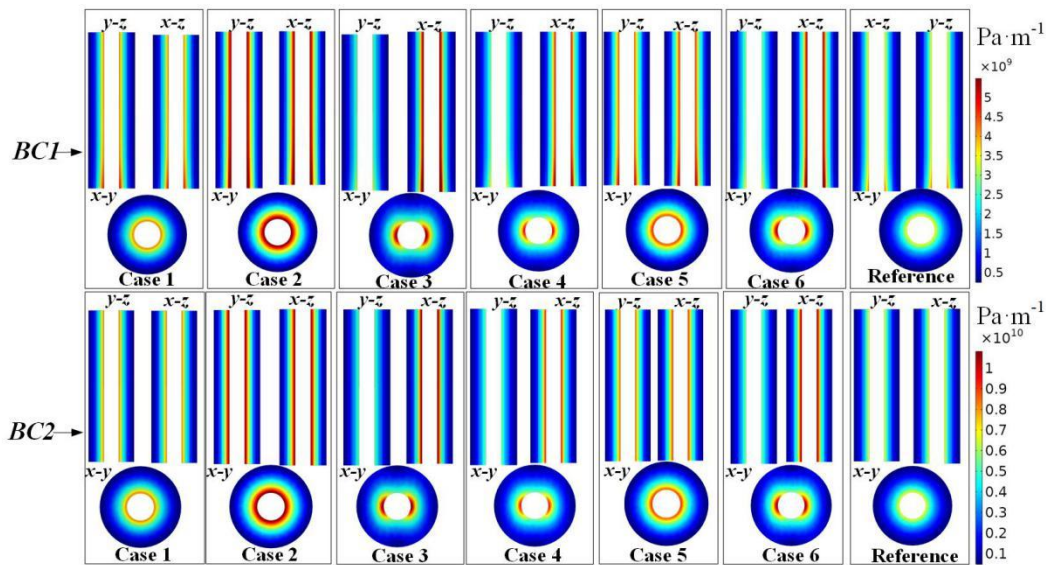


252  
 253 Fig. 4 Establishment of the osteon model (a) and mesh generation (b).

### 254 3. Results

255 As shown in Fig. 5, the distribution of pressure gradient (PG) magnitude in the  
 256 osteon under different boundary conditions at  $t = 0.25$ s was plotted. PG refers to the  
 257 change in pressure per unit length along the direction of fluid flow. It is one of the  
 258 main driving forces of fluid flow and other effects (FSS, streaming potential, and  
 259 solute transport) in the osteon [3, 4, 34, 35]. Under the axial symmetrical load, the  
 260 distribution of the PG magnitude in Case 1–Case 6 was different from that in the

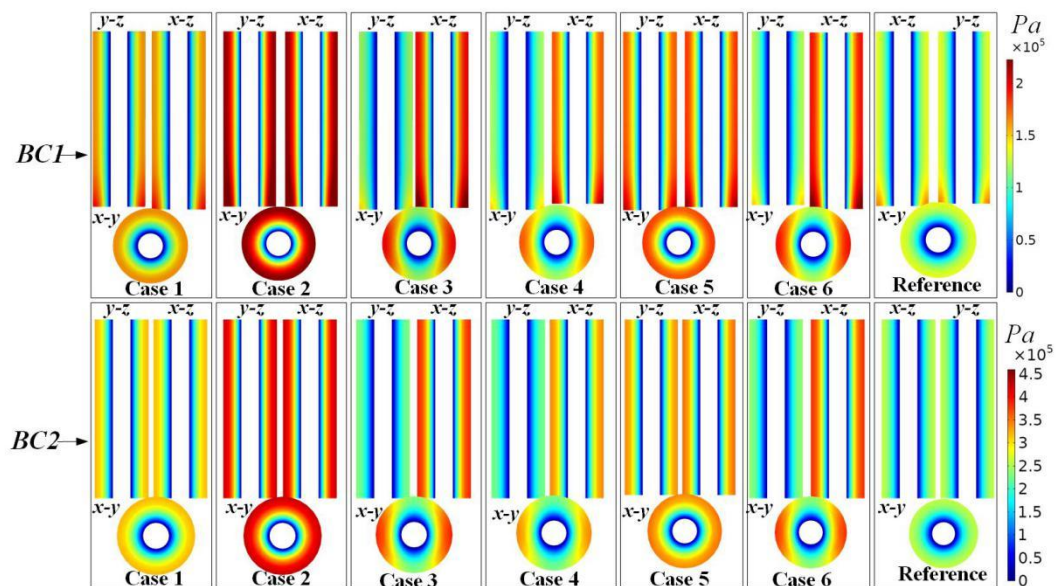
261 reference model, but the values were in same order of magnitude. The maximum PG  
 262 in Case 1–Case 6 was  $5.49 \times 10^9$  Pa/m in BC1, whereas it was  $3.3 \times 10^9$  Pa/m in the  
 263 reference model. The maximum PG in Case 1–Case 6 was 61.95% larger than that in  
 264 the reference model. The maximum PG in Case 1–Case 6 in BC2 was  $1.08 \times 10^{10}$  Pa/m,  
 265 whereas it was  $6.53 \times 10^9$  Pa/m in the reference model. The maximum PG in Case  
 266 1–Case 6 was 65.39% larger than that in the reference model. This showed that the  
 267 osteocyte shape affects the distribution of PG magnitude under the same osteocyte  
 268 volume, indicating that when the volume of the osteocyte was the same, circular  
 269 osteocytes exhibited smaller PP and FV. As shown in Fig. 6 and Fig. 7, the  
 270 distribution of PP and FV along the y-z and x-z planes in Case 1, Case 2, and Case 5  
 271 was similar, and this distribution was similar to that in the reference model. Therefore,



272  
 273 Fig. 5 The magnitude of pressure gradient distribution under different boundary  
 274 conditions at  $t = 0.25$  s. BC1: elasticity restrained. BC2: displacement constrained.  
 275 the three dimensional distribution of bone canalicules of elongated osteocytes were  
 276 more likely to cause the anisotropy of fluid flow in the bone. The maximum value of  
 277 PG in BC2 was about twice that in BC1. This indicated that the right choice of

278 boundary conditions is essential for understanding fluid flow in the bone.

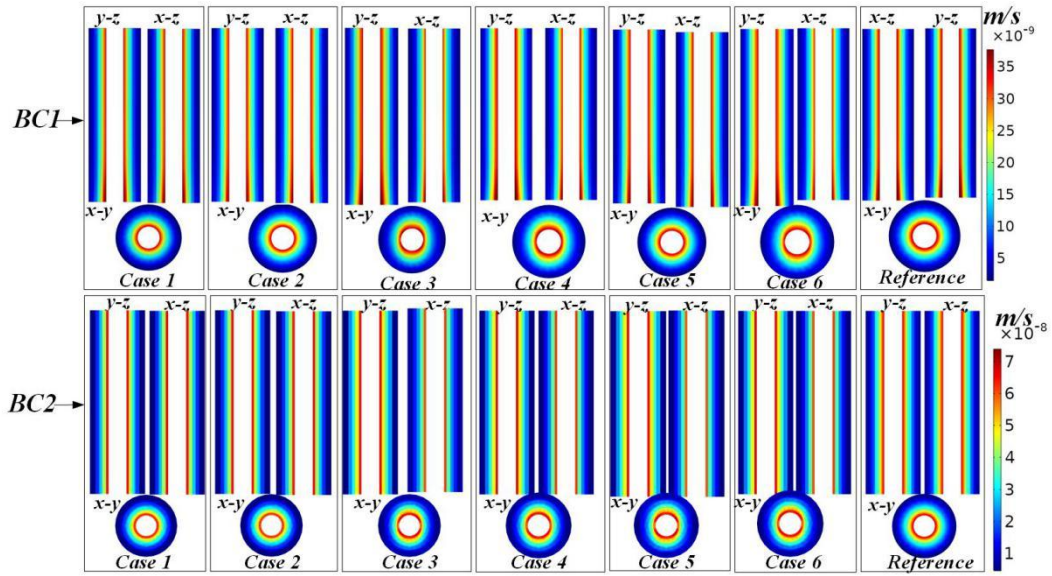
279 Fig. 6 and Fig. 7 respectively show the distribution of PP and FV under different  
280 boundary conditions. Due to the different shapes of the osteocyte, the distribution of  
281 the PP and FV in Case 1–Case 6 was significantly different from that in the reference  
282 model. Fig. 6 shows that the maximum PP value ( $2.23 \times 10^5$  Pa) in Case 1–Case 6 in BC1  
283 was 67.67% larger than that in the reference model ( $1.33 \times 10^5$  Pa). The maximum PP  
284 value ( $4.36 \times 10^5$  Pa) of Case 1–Case 6 in BC2 was 67.67% larger than that in the  
285 reference model ( $2.58 \times 10^5$  Pa). The maximum PP in BC2 was 95.51% higher than that  
286 in BC1. Fig. 7 shows that the maximum FV value ( $3.76 \times 10^{-8}$  m/s) in Case 1–Case 6 in  
287 BC1 was 8.6% larger than that in the reference model ( $3.46 \times 10^{-8}$  m/s). The maximum  
288 FV value ( $7.44 \times 10^{-8}$  m/s) in Case 1–Case 6 in BC2 was 8.4% larger than that in the  
289 reference model ( $6.86 \times 10^{-8}$  m/s). The maximum FV value in BC2 was 97.87% larger  
290 than that in BC1.



291

292 Fig. 6 The magnitude of pore pressure distribution under different boundary  
293 conditions at  $t = 0.25$  s. BC1: elasticity restrained. BC2: displacement constrained.

294



295

296 Fig. 7 The magnitude of flow velocity distribution under different boundary  
 297 conditions at  $t = 0.25$  s. BC1: elasticity restrained. BC2: displacement constrained.

298

299 Fig. 8 shows the distribution of FSS in the osteon with different osteocyte shapes  
 300 at  $t = 0.25$  s. Fig. 7 and Fig. 8 show similar trends in spatial distribution. In BC1, the  
 301 maximum FSS value in Case 1–Case 6 was 3.83 Pa, whereas it was 3.0 Pa in the  
 302 reference model. In BC2, the maximum FSS value in Case 1–Case 6 was 7.55 Pa,  
 303 whereas it was 5.85 Pa in the reference model. Thus, a change in osteocyte shape  
 304 would make the maximum FSS value 26.6% and 29% larger than that in the reference  
 305 model in BC1 and BC2, respectively.

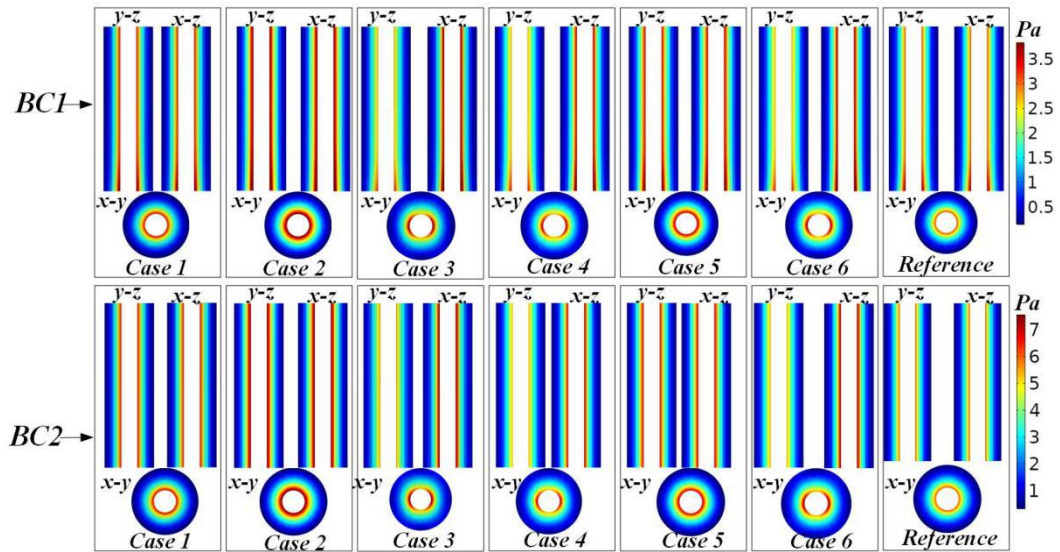


Fig. 8 The magnitude of fluid shear stress distribution under different boundary conditions at  $t = 0.25$  s. BC1: elastic restrained. BC2: displacement constrained.

#### 4. Discussion

In this study, poroelastic finite element models were developed to investigate the effect of osteocyte shape on fluid flow and FSS in osteons under different boundary conditions. These models were established based on the osteon microstructure to simulate interstitial fluid flow arising from the mechanical deformation of the osteon and PGs under axial loading representative of physical activity. For modeling purposes, we assumed that the osteons were composed of CPUC, and then we estimated the permeability and porosity of the osteon by estimating the number and three-dimensional distribution of bone canaliculi in different shapes of the bone lacuna.

PG refers to the change in pressure per unit length along the direction of fluid flow. Previous studies have often not discussed this vital parameter [3, 18, 22, 34].

322 Mechanical loading in the osteon occurs at the whole -organ level, with compression  
323 and tension occurring in different regions, driving fluid flow in the lacunar-canalicular  
324 network [36]. Maximal PP occurs at the cement line. Because of low blood pressure  
325 in Haversian canal boundary, the PP magnitudes maintained to be at a lower level.  
326 Therefore, a PG established across the osteon wall should be large enough to drive  
327 fluid against the trans-cortical pressure difference [21]. In this study, the trans-cortical  
328 pressure difference was at least  $1.33e5$  Pa and  $2.58e5$  Pa in the reference model in  
329 BC1 and BC2, respectively, and the PG was sufficient (at least  $3.3e9$  Pa/m and  $6.53e9$   
330 Pa/m) to counter the trans-cortical pressure difference. As shown in Fig. 5, the PG  
331 decreased dramatically away from the Haversian canal. As a result osteocytes far  
332 away from the Haversian canal had significantly lower FSS than osteocytes relatively  
333 close to the Haversian canal (Fig. 8).

334 PP is an essential load -inducing phenomenon in the lacunar-canalicular network,  
335 which affects the growth, differentiation, and material transport of osteocytes [3, 4, 21,  
336 37]. The PP changed significantly with osteocyte shape. Specifically, the distribution  
337 of PP between Case 3, Case 4, and Case 6 in the x and y directions was markedly  
338 asymmetric, whereas it was axisymmetric in Case 1, Case 2, Case 5, and the reference  
339 model in x and y directions in both BC1 and BC2. This shows the anisotropy of  
340 permeability induced by the change in osteocyte shape. The permeability of Case 3,  
341 Case 4, and Case 6 models was one order of magnitude different in the x and y  
342 directions, whereas the permeability of Case 1 Case 2, Case 5, and the reference  
343 model in the x and y directions showed little difference. In the z direction, the PP of

344 all models did not change substantially. This is because the mechanism of load  
345 -induced PP makes the fluid flow into the Haversian canal through the  
346 lacunar-canalicular network and release the PP [21]. Therefore, the main fluid flow of  
347 osteon is between the cement line and the Haversian canal, and there is almost no  
348 fluid flow in the z direction. As shown in Fig. 5, Fig. 6, Fig. 7, and Fig. 8, different  
349 boundary conditions have significant effects on the flow behavior in the osteon. The  
350 maximum PG, PP, FV, and FSS in BC2 were 96.72%, 95.51%, 97.87%, and 97.13%  
351 larger than those in BC1, respectively.

352 In BC1, some physiological pressure generated outside the osteon can neutralize  
353 the PP of the osteon, and the outer wall of the osteon is not constrained by the  
354 interstitial tissue around the osteon. Therefore, the outer wall of the osteon is only  
355 affected by the fluid pressure in the interstitial tissue. In BC2, the cement line of the  
356 osteon is constrained by the interstitial tissue around the osteon and cannot move, and  
357 and none fluid be allowed across the outer restraint boundary. Some studies have  
358 observed that there are bone canaliculi passing through the cement line [19, 38],  
359 which indicates that the cement line is indeed permeable and that fluid exchange  
360 between the osteon and the external interstitial bone is possible. Therefore, BC1  
361 seems to more closely mimic the physiological state than BC2.

362 Verbruggen et al. observed the mean interstitial FV ( $\sim 60.5 \mu\text{m/s}$ ) and the mean  
363 maximum FSS ( $\sim 11 \text{ Pa}$ ) around osteocytes in vivo by applying a load (3000  $\mu\text{e}$   
364 compression and 300 Pa PG) representing strong physiological activity [9]. Our result  
365 for BC2 was similar to their result; however, the loading in BC2 represents normal

366 physiological activities. Some studies considered that the FSS level required for bone  
367 growth is 0.8 Pa [9, 39]. FSS in the range of 0.1–2.2 Pa can increase the production  
368 of nitric oxide, prostaglandin, and osteopontin [6, 9]. An FSS of 2 Pa can increase  
369 intracellular calcium ( $\text{Ca}^{2+}$ ), and an FSS of 0.2–6 Pa can induce cell response [8, 9].  
370 Our results (~3.83 Pa in BC1 and ~7.55 Pa in BC2) suggest that the fluid slow  
371 stimulating the osteocytes was sufficient to elicit biochemical signals for bone  
372 formation. Similar FSS values (~5 Pa) have also been suggested by tracer studies [5,  
373 9]. Our findings reveal that osteocyte shape significantly influences the osteocyte  
374 fluid flow.

375 One limitation of our research is that the canaliculus was idealized as a straight  
376 tube. This study does not consider the effect of the curvature of the canaliculus, while  
377 in fact, the processes of osteocytes extend through the curved canaliculus from the  
378 osteocyte body to the surface of CUPC [9, 35]. Another limitation is that the osteon  
379 was considered to be composed of identical CUPC. The shape of the osteocyte in each  
380 CUPC may be different, which will lead to a change in the local fluid flow.  
381 Theoretically, it is necessary to determine the shape of osteocytes in each CUPC;  
382 however, it is observed in the experiment that the shape of bone lacuna is similar in a  
383 certain region of bone tissue, and such a region is large enough to contain one or  
384 several osteons [24]. Therefore, as long as the osteocyte shape in a specific region of  
385 bone is determined, the method of this study can be applied to analyze the load  
386 -induced FSS and other fluid flow behaviors.

## 387 **5. Conclusion**

388 In this study, a method was proposed to estimate the anisotropic permeability of  
389 the lacunar-canalicular network based on the shape of osteocytes. The fluid flow in  
390 the osteon was described under different boundary conditions according to the  
391 calculated permeability. Changes in osteocyte shape (Case 1–Case 6) make the  
392 maximum value of PG, PP, FV, and FSS 33.36%, 67.67%, 8.6%, and 26.6% larger  
393 than those in the reference model in BC1 and 65.39%, 67.67%, 8.4%, and 29% larger  
394 than those in the reference model in BC2, respectively. The maximum PG, PP, FV,  
395 and FSS in BC2 were 96.72%, 95.51%, 97.87%, and 97.13% larger than those in BC1,  
396 respectively. The permeability of Case 3, Case 4, and Case 6 had a difference of one  
397 magnitude order in the x and y directions, indicating that elongated osteocytes are  
398 more likely to cause anisotropy of permeability. The findings of this study reveal the  
399 importance of understanding the mechanotransduction in the bone, which will help us  
400 better assess some bone diseases such as osteoporosis.

### 401 **Authors' contributions**

402 All authors have made substantial contributions to the conception of the methodology.  
403 All the authors listed have approved the manuscript.

### 404 **Ethics approval and consent to participate**

405 Not applicable.

### 406 **Consent for publication**

407 Not applicable.

## 408 **Availability of data and material**

409 Data are available from the corresponding author upon reasonable request.

## 410 **Competing interests**

411 No conflict of interest exists in the submission of this manuscript.

## 412 **Funding**

413 This dissertation is supported by the Doctoral Program Foundation of Jilin  
414 Medical University JYBS2021025LK

## 415 **Acknowledgements**

416 The authors would like to thank all the reviewers who participated in the  
417 review and MJEditor ([www.mjeditor.com](http://www.mjeditor.com)) for its linguistic assistance during the  
418 preparation of this manuscript.

419

## 420 **6. Reference**

- 421 [1] T. Ganesh, L.E. Laughrey, M. Niroobakhsh, N. Lara-Castillo, Multiscale finite element  
422 modeling of mechanical strains and fluid flow in osteocyte lacunocanalicular system, *Bone*,  
423 2020,137, 115328, DOI: 10.1016/j.bone.2020.115328
- 424 [2] H.Y. Stevens, D.R. Meays, J.A. Frangos, Pressure gradients and transport in the murine  
425 femur upon hindlimb suspension, *Bone*, 2006,39, 565-572, DOI :  
426 10.1016/j.bone.2006.03.007
- 427 [3] X. Wu, C. Li, K. Chen, Y. Sun, W. Chen, Multi-scale mechanotransduction of the  
428 poroelastic signals from osteon to osteocyte in bone tissue, *Acta Mechanica Sinica*,  
429 2020,36, 1-17, DOI: 10.1007/s10409-020-00975-y
- 430 [4] Z.H. Jin, J.G. Janes, M.L. Peterson, A Chemo-poroelastic Analysis of Mechanically  
431 Induced Fluid and Solute Transport in an Osteonal Cortical Bone, *Ann. Biomed. Eng.*,  
432 2020, DOI: 10.1007/s10439-020-02544-7

- 433 [5] C. Price, X. Zhou, W. Li, L. Wang, Real - time measurement of solute transport within the  
434 lacunar - canalicular system of mechanically loaded bone: Direct evidence for load -  
435 induced fluid flow, *Journal of Bone and Mineral Research*, 2011,26, DOI :  
436 10.1002/jbmr.211.
- 437 [6] R.G. Bacabac, T.H. Smit, M.G. Mullender, S.J. Dijcks, J. Loon, J. Klein-Nulend, Nitric oxide  
438 production by bone cells is fluid shear stress rate dependent, *Biochem. Biophys. Res.*  
439 *Commun.*, 2004,315, 823-829, DOI: 10.1016/j.bbrc.2004.01.138.
- 440 [7] S. Weinbaum, S.C. Cowin, Y. Zeng, A model for the excitation of osteocytes by mechanical  
441 loading-induced bone fluid shear stresses, *J. Biomech.*, 1994,27, 339-360, DOI :  
442 10.1016/0021-9290(94)90010-8.
- 443 [8] X. Wu, N. Wang, Z. Wang, W. Yu, Y. Wang, Y. Guo, W. Chen, Mathematically modeling  
444 fluid flow and fluid shear stress in the canaliculi of a loaded osteon, *Biomed. Eng. Online*,  
445 2016,15, 149, DOI: 10.1186/s12938-016-0267-x.
- 446 [9] S.W. Verbruggen, T.J. Vaughan, L.M. Mcnamara, Fluid flow in the osteocyte mechanical  
447 environment: a fluid-structure interaction approach, *Biomech. Model. Mechanobiol.*,  
448 2014,13, 85-97, DOI: 10.1007/s10237-013-0487-y.
- 449 [10] E.L. George, S.L. Truesdell, A.L. Magyar, M.M. Saunders, The effects of mechanically  
450 loaded osteocytes and inflammation on bone remodeling in a bisphosphonate-induced  
451 environment, *Bone*, 2019,127, ,J.Y. Ru, Y.F. Wang, Osteocyte apoptosis: the roles and  
452 key molecular mechanisms in resorption-related bone diseases, *Cell Death Dis.*, 2020,11,  
453 DOI: 10.1016/j.bone.2019.07.008.
- 454 [11] T. Sun, Z. Yan, J. Cai, X. Shao, D. Jing, Effects of mechanical vibration on cell  
455 morphology, proliferation, apoptosis, and cytokine expression/secretion in osteocyte -  
456 like MLO - Y4 cells exposed to high glucose, *Cell Biol. Int.*, 2020, DOI :  
457 10.1002/cbin.11221.
- 458 [12] P.S. Vezzeridis, C.M. Semeins, Q. Chen, J. Klein-Nulend, Osteocytes subjected to  
459 pulsating fluid flow regulate osteoblast proliferation and differentiation, *Biochem Biophys*  
460 *Res Commun*, 2006,348, 1082-1088, DOI: 10.1016/j.bbrc.2006.07.146.
- 461 [13] T.J. Vaughan, C.A. Mullen, S.W. Verbruggen, L.M. Mcnamara, Bone cell  
462 mechanosensation of fluid flow stimulation: a fluid-structure interaction model  
463 characterising the role integrin attachments and primary cilia, *Biomechanics&Modeling in*  
464 *Mechanobiology*, 2015, DOI: 10.1007/s10237-014-0631-3.
- 465 [14] M. Martin, V. Sansalone, D. Cooper, M.R. Forwood, P. Pivonka, Mechanobiological  
466 osteocyte feedback drives mechanostat regulation of bone in a multiscale computational  
467 model, *Biomech. Model. Mechanobiol.*, 2019,18, 1475-1496, DOI :  
468 10.1007/s10237-019-01158-w.
- 469 [15] M.N. An, C.R. Jacobs, Emerging Role of Primary Cilia as Mechanosensors in Osteocytes,  
470 *Bone*, 2012, 54, 196-204, DOI: 10.1016/j.bone.2012.11.016.
- 471 [16] S. Liu, F. Wang, R. Liu, Fluid flow and fluid shear stress in canaliculi induced by external  
472 mechanical loading and blood pressure oscillation, *应用数学和力学: 英文版*, 2015,36, 12,  
473 DOI: 10.1007/s10483-015-1932-7.
- 474 [17] L. Cardoso, S.P. Fritton, G. Gailani, M. Benalla, S.C. Cowin, Advances in assessment of  
475 bone porosity, permeability and interstitial fluid flow, *J. Biomech.*, 2013,46, 253-265, DOI:  
476 10.1016/j.jbiomech.2012.10.025.

- 477 [18] Y. Chen, W. Wang, S. Ding, W. Xu, Q. Chen, L. Xing, A multi-layered poroelastic slab  
478 model under cyclic loading for a single osteon, *Biomedical Engineering Online*, 2018,17,  
479 97, DOI: 10.1186/s12938-018-0528-y.
- 480 [19] V.H. Nguyen, T. Lemaire, S. Naili, Poroelastic behaviour of cortical bone under harmonic  
481 axial loading: A finite element study at the osteonal scale, *Med. Eng. Phys.*, 2010,32,  
482 384-390, DOI: 10.1016/j.medengphy.2010.02.001.
- 483 [20] X.G. Wu, W.Y. Chen, A hollow osteon model for examining its poroelastic behaviors:  
484 Mathematically modeling an osteon with different boundary cases, *European Journal of*  
485 *Mechanics - A/Solids*, 2013,40, 34–49, DOI: 10.1016/j.euromechsol.2012.12.005.
- 486 [21] G.C. Goulet, D. Coombe, R.J. Martinuzzi, R.F. Zernicke, Poroelastic Evaluation of Fluid  
487 Movement Through the Lacunocanalicular System, *Ann. Biomed. Eng.*, 2009,37,  
488 1390-1402, DOI: 10.1007/s10439-009-9706-1.
- 489 [22] X. Wu, K. Chen, Z. Wang, N. Wang, T. Zhao, Y. Xue, Y. Wang, W. Chen, An analytical  
490 poroelastic model for laboratorial mechanical testing of the articular cartilage (AC),  
491 *Applied Mathematics and Mechanics(English Edition)*, 2018,39, 813-828, DOI :  
492 10.1007/s10483-018-2334-9.
- 493 [23] E. Alizadeh, M. Dehestani, P. Zysset, An efficient two-scale 3D FE model of the bone fibril  
494 array: comparison of anisotropic elastic properties with analytical methods and  
495 micro-sample testing, *Biomech. Model. Mechanobiol.*, 2020,19, DOI :  
496 10.1007/s10237-020-01328-1.
- 497 [24] Y. Carter, C. Thomas, J.G. Clement, A.G. Peele, K. Hannah, D. Cooper, Variation in  
498 osteocyte lacunar morphology and density in the human femur – a synchrotron radiation  
499 micro-CT study, *Bone*, 2013,54, 126-132, DOI: 10.1016/j.bone.2012.09.010.
- 500 [25] V. Wu, R. Oers, E. Schulten, M.N. Helder, R.G. Bacabac, J. Klein-Nulend, Osteocyte  
501 morphology and orientation in relation to strain in the jaw bone, *International Journal of*  
502 *Oral Science*, 2018,10, 40-47, DOI: 10.1038/s41368-017-0007-5.
- 503 [26] A. Egl, A. Mb, B. Mbg, B. Jms, A. Jlb, Human mesenchymal stem cell morphology,  
504 migration, and differentiation on micro and nano-textured titanium, *Bioactive Materials*,  
505 2019,4, 249-255, DOI: 10.1016/j.bioactmat.2019.08.001.
- 506 [27] T. Ishimoto, K. Kawahara, A. Matsugaki, J. Wang, H. Kamioka, T. Nakano, Analysis of  
507 Osteocyte Morphology in Terms of Sensation of In Vivo Stress Applied on Bone, *Mater.*  
508 *Sci. Forum*, 2014, pp. 1265-1268,  
509 DOI:https://doi.org/10.4028/www.scientific.net/MSF.783-786.1265.
- 510 [28] S.W. Verbruggen, T.J. Vaughan, L.M. McNamara, Mechanisms of osteocyte stimulation in  
511 osteoporosis, *J. Mech. Behav. Biomed. Mater.*, 2016,62, 158-168, DOI :  
512 10.1016/j.jmbbm.2016.05.004.
- 513 [29] H. Hemmatian, A.D. Bakker, J. Klein-Nulend, G. Lenthe, Aging, Osteocytes, and  
514 Mechanotransduction, *Current Osteoporosis Reports*, 2017,15, 1-11, DOI :  
515 10.1007/s11914-017-0402-z.
- 516 [30] T. Rolvien, F.N. Schmidt, P. Milovanovic, K. Jhn, C. Riedel, S. Butscheidt, K. Püschel, A.  
517 Jeschke, M. Amling, B. Busse, Early bone tissue aging in human auditory ossicles is  
518 accompanied by excessive hypermineralization, osteocyte death and micropetrosis, *Sci.*  
519 *Rep.*, 2018,8, 1920, DOI: 10.1038/s41598-018-19803-2.

- 520 [31] T. Beno, Y.-J. Yoon, S.C. Cowin, S.P. Fritton, Estimation of bone permeability using  
521 accurate microstructural measurements, *J. Biomech.*, 2006,39, 2378-2387, DOI :  
522 10.1016/j.jbiomech.2005.08.005.
- 523 [32] N.K. Wittig, M. Laugesen, M.E. Birkebæk, F.L. Bach-Gansmo, H. Birkedal, Canalicular  
524 Junctions in the Osteocyte Lacuno-Canalicular Network of Cortical Bone, *ACS Nano*,  
525 2019,13, DOI: 10.1021/acsnano.8b08478.
- 526 [33] M. Benalla, P.E. Palacio-Mancheno, S.P. Fritton, L. Cardoso, S.C. Cowin, Dynamic  
527 permeability of the lacunar-canalicular system in human cortical bone, *Biomech. Model.*  
528 *Mechanobiol.*, 2013,13, 801-812, DOI: 10.1007/s10237-013-0535-7.
- 529 [34] Y. WeiLun., W. XiaoGang., C. HaiPeng., G. Yuan., L. ChaoXin., W. YanQin., Q. YiXian., C.  
530 WeiYi., Study on the biomechanical responses of the loaded bone in macroscale and  
531 mesoscale by multiscale poroelastic FE analysis, *Biomed. Eng. Online*, 2019,18, DOI:  
532 10.1186/s12938-019-0741-3.
- 533 [35] A. Tol, A. Roschger, F. Repp, J. Chen, R. Weinkamer, Network architecture strongly  
534 influences the fluid flow pattern through the lacunocanalicular network in human osteons,  
535 *Biomech. Model. Mechanobiol.*, 2020,19, 823-840, DOI: 10.1007/s10237-019-01250-1.
- 536 [36] M. Tate, "Whither flows the fluid in bone?" An osteocyte's perspective, *J. Biomech.*,  
537 2003,36, 1409-1424, DOI: 10.1016/S0021-9290(03)00123-4.
- 538 [37] G. Gailani, S. Cowin, THEORETICAL ANALYSIS OF THE LEAKAGE THROUGH THE  
539 CEMENT LINE OF A SINGLE OSTEON, *Journal of Mechanics in Medicine and Biology*,  
540 2020,20, 950073, DOI: 10.1142/S0219519419500738.
- 541 [38] D. Yin, B. Chen, S. Lin, Finite element analysis on multi-toughening mechanism of  
542 microstructure of osteon, *J. Mech. Behav. Biomed. Mater.*, 2021,117, 104408, DOI:  
543 10.1016/j.jmbbm.2021.104408.
- 544 [39] Y. Han, S.C. Cowin, M.B. Schaffler, S. Weinbaum, Mechanotransduction and strain  
545 amplification in osteocyte cell processes, *Proceedings of the National Academy of*  
546 *Sciences*, 2004,101, 16689-16694, DOI: 10.1073/pnas.0407429101.